Design of the photonic crystal fiber-based surface plasmon resonance sensors

Yang Peng (彭 杨)*, Jing Hou (侯 静), Zhihe Huang (黄值河), Bin Zhang (张 斌), and Qisheng Lu (陆启生)

College of Optoelectronic Science and Engineering, National University of Defense Technology, Changsha 410073, China

**Corresponding author: pynudt@yahoo.com.cn*

Received November 30, 2011; accepted February 26, 2012; posted online June 20, 2012

The photonic crystal fiber-based surface plasmon resonance (SPR) refractive index sensor is demonstrated by using post-processing technique of photonic crystal fiber (PCF). The coupling of PCF mode field and SPR can be controlled by the air holes collapsing in PCF. The effects of metal film thickness and air hole diameter on the sensor at different wavelength are simulated by using finite element method. The simulation results are analyzed by using the modes matching theory. The amplitude based and spectrum based detection methods are discussed respectively. Refractive index sensitivity 1 700 nm/per refractive index unit (RIU) can be achieved for an aqueous analyte.

OCIS codes: 060.5295, 060.2370, 240.6680.

doi: 10.3788/COL201210.S10607.

Propagating at the metal/dielectric interface, surface plasmons[1] are extremely sensitive to the changes in refractive index of the dielectric. This feature of surface plasmon resonance (SPR) has been used for sensor systems for a long time[2]. The research of fiber-optic SPR sensors began in the early 1990 s. The real fiber SPR sensors that use fiber devices as sensor heads were first proposed in 1993[3]. The fiber SPR sensor offers high sensitivity, miniaturization, high degree of integration and remote sensing capabilities. Since then, driven by the need for miniaturization of SPR sensors, various optical fiber SPR sensors have been investigated. The SPR fiber sensor has the capacity to detect changes in external refractive index. It can be optimized by adjusting parameters such as the thickness of the metal layer and over-layer, etc.[2,4]. Several theoretical as well as experimental studies have been carried out, in attempts to improve the performance of fiber-optic SPR sensors.

SPR fiber sensors can have diverse structures such as D-shape, cladding-off, fiber tip, or tapered fiber structures[5−7]. Some novel SPR based fiber-optic sensors have also been proposed, such as fiber sensor adopting cascaded long period gratings (LPGs)[8], SPR fiber sensor with a fiber Bragg grating (FBG)[9]. With the progress in micro-structure fiber technologies, Hassani *et al.* proposed the concept for a micro-structured optical fiber-based SPR sensor with optimized micro-fluidics, which has a sensitivity of 10^{-4} RIU leads to a 1% change in the intensity of the transmitted light[10].

The progress of fiber SPR sensor is very close to the development of fiber. During the fiber SPR sensor researching, the fabrication and cost are very important. With the development of post-processing technique of photonic crystal fiber, a fiber SPR sensor based on PCF is demonstrated in this letter. The mode field of PCF can be accurately changed by hole collapse[11−13]. After partially removing the fiber cladding by chemical etching[14], precise flame controlling[15], or polishing and coating it with metal, the mode field of PCF and SPR can be coupled. Performance of the PCF-SPR sensors can be optimized by adjusting the thickness of the metal layer, over-layer, and the air-hole diameter.

The schematic of a PCF-SPR sensor developed in this letter is shown in Fig. 1. Air holes in PCF can be collapsed when the PCF is heated due to the surface tension. The defining parameters of the structure are thus the physical pitch (distance between the nearest neighbour air holes) which we denote Λ, the air hole diameter d. Λ_0, d_0 are the initial values of pitch and hole size, respectively. Λ, d are the values of pitch and hole size after collapse, respectively. We assume that the pitch decreases during the hole collapse so that the total silica area remains constant. The relation of the parameters is[11]

$$(\Lambda/\Lambda_0)^2 = \frac{\sqrt{3}/2 - \pi/4\,(d_0/\Lambda_0)^2}{\sqrt{3}/2 - \pi/4\,(d/\Lambda)^2}. \tag{1}$$

The energy loss is very low if the transition connected the original PCF and the collapsed section of PCF is adiabatic. The collapse of air holes can effectively increase the mode field diameter (MFD) of PCF. In Fig. 1, the gray parts show the mode areas of the PCF guided modes. Firstly we decrease the thickness of the cladding by chemically etching or polishing to reduce the distance between the outermost air holes and the external environment and then coat the cladding with metallic film. The coupling of mode field of PCF and SPR can be controlled by controlling the collapse of the air holes in PCF. And it is easy to integrate this sensor with other fiber device with very low energy loss. By using the sensitivity of SPR to refractive index, we can measure the refractive index changes of the external environment by measuring the variation of intensity or spectrum.

The air hole diameter of the silica PCF is 1 μm, the pitch is 3 μm, the diameter of the fiber is 14 μm. There are two layers of air holes in the fiber. After collapse, the air hole diameter decreases to 400 nm, the pitch increases and the diameter of the fiber decreases correspondingly. Then we coat the cladding with metallic film of 40 nm thicknesses as shown in Fig. 1. The range of dispersion relation data of silica is from 0.21 to 3.71 μm[16]

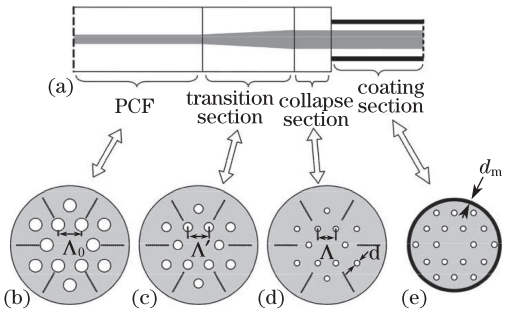

Fig. 1. Structure of a PCF-SPR sensor. (a) The side view of the sensor. The gray parts show the mode areas of the PCF guided modes. (b) Cross section of the original PCF. The light grey areas are silica, the white areas are air holes. (c) Cross section of the transition section of sensor. (d) Cross section of collapse section. There are more than two layers of air holes in (b), (c), and (d). (e) Cross section of the coating section of sensor. The black areas are metallic coating. Two layers of air holes are left in this section.

and the dispersion relation data of silver is from CRC Handbook of Chemistry and Physics[17].

Commercial software COMSOL Multiphysics was used to simulate the PCF-SPR sensor. The effective refractive indexes ($n_{\rm eff}$) of the modes were calculated at different wavelengths. The imaginary part of $n_{\rm eff}$ denotes the loss of the mode. The loss coefficient in decibels per centimeter is defined by $\alpha({\rm dB/cm})=40\pi{\rm lg}(e){\rm Im}(n_{\rm eff})/\lambda$, where λ is in centimeter.

The fundamental modes dispersion curves of PCF-SPR sensor and PCF without metallic film are shown in Fig. 2(a). The analyte refractive indexes are 1.33 and 1.34, respectively. The dispersion curves are very close at short wavelength. In Fig. 2(b) we show the losses of fundamental modes in the wavelength range of 0.4−2 μm for two values of analyte refractive indices n_a=1.33 and n_a=1.34. The loss of PCF without metallic film is less than 10^{-10} dB/cm. Loss of the fundamental mode increases with wavelength because the increasing of metal absorbability and confinement loss. Loss curves in Fig. 2(b) feature two obvious plasmonic peaks located at 500 nm and 1 700 nm. Compared with the other peaks, 500 nm peak is more sensitive to the changes in the analyte refractive index.

Mode coupling theory is used to analyze the simulation results. Dispersion curve of the PCF without metallic film was simulated at first. Then we see the fiber as a dielectric cylinder. The dispersion relations of surface palsmon modes guided on silver-silica surface and silver-analyte surface are calculated. The dispersion curves of v=0 to v=5 orders silica bound plasmon modes (excitated on the surface between silver and silica cylinder) are shown in Fig. 3(a). The dispersion curves of analyte bound plasmon modes (excitated on the surface between silver and analyte) are very close at the short wavelength and we draw only one curve in Fig. 3(a). Figures 3(b) and (c) shows the flux distributions of fundamental modes at 494-nm and 1 642-nm wavelength when the silver film thickness of the PCF-SPR sensor is 40 nm and the air hole diameter is 400 nm. To represent flux distributions around the metal film obviously, Figures 3(d) and (e) show the intensity in the pane in Figs. 3(b) and (c).

In Fig. 3(a), dispersion curve of fundamental mode of PCF without metallic film intersect the dispersion curves of surface plasmon modes at about 500 nm. According to Fig. 2(b), we consider the 500 nm plasmonic peak is generated by the excitation of analyte bound plasmon modes. The mode in PCF is coupled to the surface plasmon modes. Consequently, analyte bound plasmon modes are affected strongly by changes in the analyte refractive index. Figure 3(d) confirms this conclusion. When wavelength is 494 nm, intensity around the analyte surface is stronger than it around cladding surface.

In Fig. 3(a), dispersion curves of v=0 to v=3 orders silica bound plasmon modes do not intersect the dispersion curve of PCF without metallic film, while higher orders ($v>3$) intersect. According to Fig. 2(b), we consider the plasmonic peaks between 1 000 nm and 2 000 nm are generated by the excitation of silica bound plasmon modes. They vary little with the changes in analyte refractive index. According to Fig. 3(c), there are ten intensity peaks on the silver-silica interface, the fifth order silica bound plasmon mode coupled with the fiber

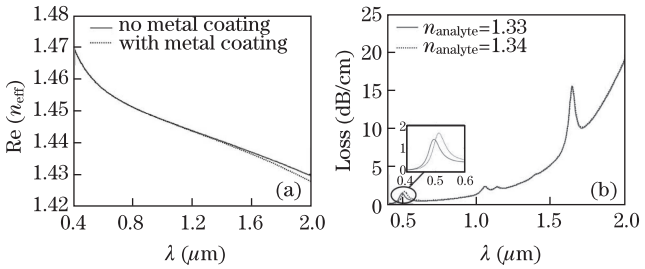

Fig. 2. (a) Solid line shows the dispersion of fundamental mode of the collapsed PCF without metal coating. Dotted line shows the dispersion of PCF after collapse and coating. (b) Calculated loss spectra of the fundamental mode of coated PCF exhibiting two loss peaks corresponding to the excitation various plasmonic modes in the metallic film.

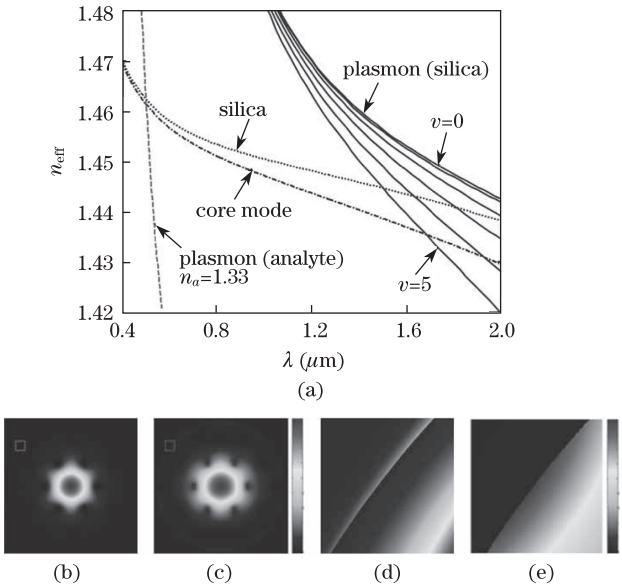

Fig. 3. (a) Dispersion relation of the fundamental core mode of PCF, silica, analyte bound plasmon mode, and silica bound plasmon mode. (b), (c) Flux distributions of the cross-section of the whole sensor at 494-nm and 1 642-nm wavelength. (d), (e) Intensity in the red pane in Figs. 3(b) and (c).

core mode when wavelength is 1 642 nm. In Fig. 3(e), intensity around cladding surface was much stronger than that around the analyte surface.

According to the simulation above, in what follows we focus on the 500 nm peak which is most sensitive to the changes in the analyte refractive index. We will analyze the changes of this peak when silver layer thickness and air hole diameter vary. The air hole diameter of the silica PCF is 1 μm, the pitch is 3 μm, the diameter of fiber is 14 μm. There are two layers of air holes in the fiber. The air hole diameter is collapsed to 300, 400, and 500 nm, respectively. The thickness of metallic film varies for 30, 40, and 50 nm.

Figure 4(a) shows the loss of the fundamental core mode near the phase matching point with the plasmon when the thickness of metallic film is 40 nm, air hole diameter is 300, 400, and 500 nm, respectively. As the air hole diameter decreases, difference of $n_{\rm eff}$ between core and cladding decreases and $n_{\rm eff}$ of the fundamental mode increases. The energy flux in cladding and metallic film is enhanced. Energies absorbed by metallic film or leaked out are increased correspondingly. The modal loss reach its maximum at the phase matching wavelength. The resonance peak rises with air hole diameter decreasing. We can see that position of the resonance peak at wavelength almost does not change. According to Fig. 3(a), this is because when the air hole diameter changes, the dispersion curve of PCF-SPR sensor and the phase matching point varies little.

Figure 4(b) presents loss of fundamental core mode near the phase matching point with the plasmon when the air hole diameter is 400 nm, thickness of metallic film varies for 30, 40, and 50 nm. As the thickness of metallic film increases, the energy through metallic film decreases and the energy of analyte bound plasmon modes is weaken.

Figure 5(a) presents the loss of the fundamental core mode near the phase matching point with the plasmon when $d_{\rm air}$=300 nm and $d_{\rm silver}$=30 nm. The position of plasmon resonance peak is at 467 nm with $n_{\rm a}$=1.33 and 482 nm with $n_{\rm a}$=1.34. Figure 5(b) presents the loss of fundamental core mode near the phase matching point with the plasmon when $d_{\rm air}$=400 nm and $d_{\rm silver}$=40 nm. The position of plasmon resonance peak is at 494 nm with $n_{\rm a}$=1.33 and 511 nm with $n_{\rm a}$=1.34.

There are two main modalities of SPR detection – the amplitude based and spectrum based[10,18]. We start by describing a single wavelength, amplitude based detection method. We define transmission loss of a core

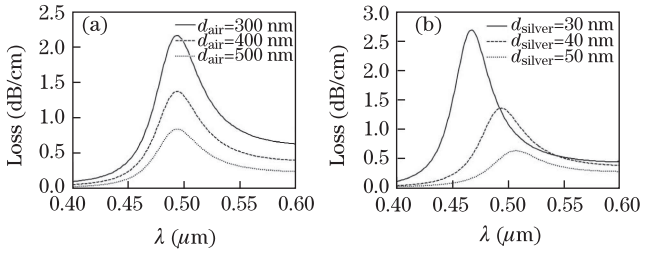

Fig. 4. (a) Calculated loss spectra of the first plasmon peak for 300, 400, and 500 nm diameter of air holes. The thickness of silver coating is 40 nm. (b) Calculated loss spectra of the first plasmon peak for 30, 40, and 50 nm thickness of a silver coating. The diameter of air hole is 400 nm.

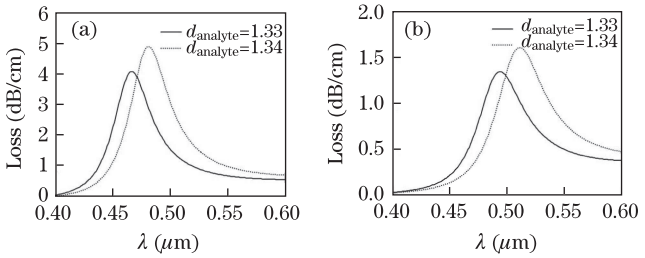

Fig. 5. Calculated loss spectra of the first plasmon peak for different structures when the refractive index of the analyte is varied. (a) Air hole diameter of 300 nm and thickness of silver coating of 30 nm. (b) Air hole diameter of 400 nm and thickness of silver coating of 40 nm.

mode as a function of wavelength and the analyte refractive index as $\alpha(\lambda,\ n_a)$. Considering P_0 to be the power launched into the fiber core mode, the detected power after propagation along the sensor of length L will be $P = P_0\ \exp[-\alpha(\lambda,\ n_{\rm a})L]$. Relative sensitivity to the $\mathrm{d}n_{\rm a}$ changes in the analyte refractive index can then be defined as

$$S_{\rm A}\left(\lambda\right)\left[\mathrm{RIU}^{-1}\right] = \left[P\left(L,\lambda,n_{\rm a}+\mathrm{d}n_{\rm a}\right) - P\left(L,\lambda,n_{\rm a}\right)\right] / q\left[P\left(L,\lambda,n_{\rm a}\right)\cdot \mathrm{d}n_{\rm a}\right]. \quad (2)$$

When we choose a sensor length L=1/α (λ, $n_{\rm a}$), the definition of sensitivity for the small changes in the analyte refractive index become

$$S_{\rm A}\left(\lambda\right)\left[\mathrm{RIU}^{-1}\right] = \frac{1}{P\left(L,\lambda,n_{\rm a}\right)}\frac{\partial P\left(L,\lambda,n_{\rm a}\right)}{\partial n_{\rm a}} = \frac{1}{\alpha\left(\lambda,n_{\rm a}\right)}\frac{\partial \alpha\left(\lambda,n_{\rm a}\right)}{\partial n_{\rm a}}. \quad (3)$$

Figure 6 shows the amplitude sensitivity of the computed PCF-SPR sensor. The maximal sensitivity is achieved at 493 nm and equals to 94.29 RIU^{-1} when $d_{\rm air}$=300 nm and $d_{\rm silver}$=30 nm. It is a typically safe assumption that a 1% change in the transmitted intensity can be detected reliably, which leads to the sensor resolution of 1.07×10^{-4} RIU. The maximal sensitivity is achieved at 524 nm and equals to 75.79 RIU^{-1} when $d_{\rm air}$=400 nm and $d_{\rm silver}$=40 nm. The sensor resolution is 1.3×10^{-4} RIU.

In the spectrum based detection method, changes in the analyte refractive index are detected by measuring the displacement of the plasmonic peak $\lambda_{\rm peak}$[18]. In this case, sensitivity is defined as

$$S_{\lambda}\left[\mathrm{nm}\cdot\mathrm{RIU}^{-1}\right] = \frac{\mathrm{d}\lambda_{\rm peak}\left(n_{\rm a}\right)}{\mathrm{d}n_{\rm a}}. \quad (4)$$

The corresponding spectral sensitivity is 1 500 nm·RIU^{-1} when $d_{\rm air}$=300 nm and $d_{\rm silver}$=30 nm. It is typically a safe assumption that a 0.1-nm change in the position of a resonance peak can be detected reliably, which leads to a sensor resolution of 6.7×10^{-5} RIU. The spectral sensitivity is 1 700 nm·RIU^{-1} and sensor resolution is 5.9×10^{-5} RIU, when $d_{\rm air}$=400 nm and $d_{\rm silver}$=40 nm.

In conclusion, we propose and numerically demonstrate a PCF-based surface plasmon resonance sensor for measuring changes in low refractive index analyte. In

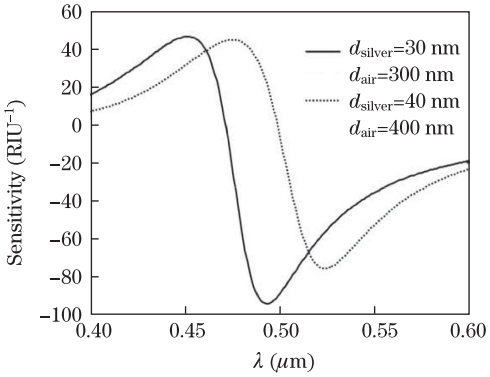

Fig. 6. Dependence of sensor amplitude sensitivity on wavelength for two different structures.

such sensors, a Gaussian-like fiber core mode is phase matched with a surface plasmon on the metal coating. Post-processing technique of photonic crystal fiber is used to optimize performance of the sensor. The coupling of PCF mode field and SPR can be controlled by the air holes collapsing in PCF. Simulation results are explained by using the modes matching theory. The amplitude sensitivity of the proposed designs could reach 94 RIU^{-1}. Assuming that a 1% change in the transmitted intensity can be detected reliably, a sensor resolution 1.07×10^{-4} RIU was demonstrated. The spectral sensitivity of the proposed designs could reach 1 700 nm·RIU^{-1}. Assuming that a 0.1-nm change can be detected reliably, a sensor resolution 5.9×10^{-5} RIU was demonstrated.

This work was supported by the Program of China for New Century Excellent Talents in University (No. NCET-08-0142) and the National Natural Science Foundation of China (Nos. 61077076, 61007037, 10904173, and 11004247).

References

1. H. Raether, *Surface Plasmas on Smooth and Rough Surface and on Gratings* (Springers-Verlag, Berlin, 1988).
2. J. Homola and M. Piliarik, *Surface Plasmon Resonance (SPR) Sensors* (Springer-Verlag, Berlin, 2006).
3. R. Jorgenson and S. Yee, Sensor. Actuator. B Chem. **12,** 213 (1993).
4. S. A. Maier, *Plasmonics*: *Fundamentals and Applications* (Springer Verlag, New York, 2007).
5. B. Lee, S. Roh, and J. Park, Opt. Fiber Tech. **15,** 209 (2009).
6. Z. Cao, L. Wu, and D. Li, Chin. Opt. Lett. **4,** 160 (2006).
7. Y. Chen, R. Zheng, Y. Lu, P. Wang, and H. Ming, Chin. Opt. Lett. **9,** 100605 (2011).
8. Y. J. He, Y. L. Lo, and J. F. Huang, J. Opt. Soc. Am. B **23,** 801 (2006).
9. G. Nemova and R. Kashyap, Opt. Lett. **31,** 2118 (2006).
10. A. Hassani and M. Skorobogatiy, Opt. Express **14,** 11616 (2006).
11. J. Laegsgaard and A. Bjarklev, Opt. Commun. **237,** 431 (2004).
12. Z. Chen, J. Hou, X. Xi, G. Sun, and Z. Jiang, Opt. Commun. **283,** 4645 (2010).
13. Y. Wang, Z. Chen, J. Hou, Q. Lu, D. Liang, B. Zhang, Y. Peng, and X. Liu, High Power Laser and Particle Beams (in Chinese) **22,** 1491 (2010).
14. M. Kanso, S. Cuenot, and G. Louarn, Plasmonics **3,** 49 (2008).
15. Z. Zhang, P. Zhao, F. Sun, G. Xiao, and Y. Wu, IEEE Photon. Tech. Lett. **19,** 1958 (2007).
16. I. Malitson, J. Opt. Soc. Am. **55,** 1205 (1965).
17. D. R. Lide, *CRC Handbook of Chemistry and Physics* (CRC Press, Boca Raton, 2004).
18. B. Gauvreau, A. Hassani, M. Fassi Fehri, A. Kabashin, and M. A. Skorobogatiy, Opt, Express **15,** 11413 (2007).